Available online at www.sciencedirect.com

SciVerse ScienceDirect

journal homepage: www.elsevier.com/locate/jmbbm

Research paper

New insights into hard phases of CoCrMo metal-on-metal hip replacements

Y. Liao^{a,*}, R. Pourzal^{a,b}, P. Stemmer^{a,b}, M.A. Wimmer^c, J.J. Jacobs^{a,c}, A. Fischer^{b,c}, L.D. Marks^a

^a Department of Materials Science and Engineering, Northwestern University, Evanston, IL 60201, USA

^b Department of Materials Science & Engineering, University of Duisburg-Essen, Germany

^c Department of Orthopedic Surgery, Rush University Medical Center, Chicago, IL, USA

ARTICLE INFO

Article history:

Received 17 January 2012

Received in revised form

9 March 2012

Accepted 15 March 2012

Published online 28 March 2012

Keywords:

CoCrMo alloy

Metal-on-metal

Hip prosthesis

Hard phases

Carbide

Precession electron diffraction

ABSTRACT

The microstructural and mechanical properties of the hard phases in CoCrMo prosthetic alloys in both cast and wrought conditions were examined using transmission electron microscopy and nanoindentation. Besides the known carbides of $M_{23}C_6$ -type ($M = Cr, Mo, Co$) and M_6C -type which are formed by either eutectic solidification or precipitation, a new mixed-phase hard constituent has been found in the cast alloys, which is composed of ~ 100 nm fine grains. The nanosized grains were identified to be mostly of $M_{23}C_6$ type using nano-beam precession electron diffraction, and the chemical composition varied from grain to grain being either Cr- or Co-rich. In contrast, the carbides within the wrought alloy having the same $M_{23}C_6$ structure were homogeneous, which can be attributed to the repeated heating and deformation steps. Nanoindentation measurements showed that the hardness of the hard phase mixture in the cast specimen was ~ 15.7 GPa, while the $M_{23}C_6$ carbides in the wrought alloy were twice as hard (~ 30.7 GPa). The origin of the nanostructured hard phase mixture was found to be related to slow cooling during casting. Mixed hard phases were produced at a cooling rate of $0.2^\circ C/s$, whereas single phase carbides were formed at a cooling rate of $50^\circ C/s$. This is consistent with sluggish kinetics and rationalizes different and partly conflicting microstructural results in the literature, and could be a source of variations in the performance of prosthetic devices in-vivo.

© 2012 Elsevier Ltd. All rights reserved.

1. Introduction

During the past decade over 200,000 hip replacements have been implanted in the United States annually, and this number is expected to increase to 572,000 by 2030 (Kurtz et al., 2007). For conventional implants currently made of metal-on-polyethylene (MOP) bearings, the generation of polyethylene wear debris leads to osteolysis and has been shown to be

a primary reason for early implant failure (Willert and Semlitsch, 1977). An alternative, CoCrMo metal-on-metal (MOM) implants complying with the ASTM F-75 standard, have been of extensive interest as an alternative to MOP bearings due to their excellent wear properties and corrosion resistance (Poggie et al., 1999). In addition, a beneficial tribological layer can be generated on the metal surfaces. Wimmer et al. reported that among 42 examined retrieved

* Corresponding author.

E-mail addresses: Yifeng.Liao@gmail.com, yifeng-liao@northwestern.edu (Y. Liao).

McKee–Farrar prostheses, 80% of them had tribological layers adhered firmly to the surfaces, which may act as solid lubricant (Wimmer et al., 2003) and is primarily graphitic carbon (Liao et al., 2011).

In addition to the Co, Cr and Mo, up to 0.35% weight percent carbon is incorporated in the alloys as carbides. These carbides significantly affect to the overall mechanical behavior of the CoCrMo alloy. It is generally agreed that fine carbide precipitates within the grains will increase the strength, while coarse ones at grain boundaries embrittle the material. Asgar and Peyton (1961) suggested that a spherical and discontinuous island carbide structure leads to the most ductility, and that carbides at grain boundaries reduce the ductility. While the overall mechanical properties are important, a CoCrMo implant is more than sufficiently strong to support the weight of a patient. The concern in a tribological system is more focused on how materials behave at the contacting surface. When two surfaces slide against each other, the load is carried by a number of asperities of nanometer to micrometer size. The wear medium, surface roughness and other extrinsic factors readily influence the friction. In a simplified model that only considers plastic deformation, the wear rate is inversely proportional to the hardness, i.e. the well-known Archard Equation (Hutchings, 1992). In a real tribological system, however, friction is much more complicated in that many other factors, including surface fracture, fatigue, grain rotation, and corrosion due to tribo-chemical reactions, can lead to loss of material. All these factors are related to the structure and chemical composition of the constituent phases and grain/phase boundaries, and their mechanical properties. For a hip replacement in service, the carbides usually serve as contact asperities in human synovial fluid due to their hard nature. Therefore the structural and mechanical properties of individual carbides directly affect the wear performance and should be carefully characterized. Wimmer et al. (2001) showed that carbides could be torn off under high local contact stresses, inducing surface fatigue by indentations and possibly lead to abrasion. The local contact stresses in such cases are dependent on the Young's modulus and hardness (Wimmer et al., 2001).

At room temperature, as-cast CoCrMo has an fcc metastable matrix due to its sluggish transformation to the stable hcp phase (Lopez and Saldivar-Garcia, 2008). Different kinds of carbides, e.g. $M_{23}C_6$, M_6C , have been reported in both cast and wrought alloys either at grain boundaries or in interdendritic regions. Asgar and Peyton (1961) examined as-cast CoCrMo and found carbides of different shapes, e.g. spherical discontinuous island-like carbides and continuous carbide films at grain boundaries. Clemow and Daniell (1979) solution treated an as-cast alloy at 1230 °C and found that interdendritic $M_{23}C_6$ carbides transformed to M_6C after 0.25 h annealing. Kilner et al. (1982) reported that the second phases of the lamellar structure in cast CoCrMo were predominantly $M_{23}C_6$ precipitates. After annealing at 1225 °C for 24–48 h, the $M_{23}C_6$ carbides dissolved into the matrix. The authors also observed long prismatic needle-like carbides which could possibly be M_7C_3 .

The carbide structure, however, has not been fully analyzed due to the complexity of the CoCrMoC system.

Conflicting results (Caudillo et al., 2002; Gomez et al., 1997; Taylor and Waterhouse, 1986) have been reported. For instance, Taylor and Waterhouse (1986) only observed a $M_{23}C_6$ blocky carbide after solution treatment at 1250 °C for 2 h using X-ray diffraction (XRD) and transmission electron microscopy (TEM). Caudillo et al. (2002) solution-treated Co alloys but did not observe any other carbide structure apart from $M_{23}C_6$. In addition to the crystallographic structure, the reported chemical compositions of carbide precipitates are conflicting. Clemow and Daniell (1979) reported that the fractions of Mo and Cr were 6% and 35%, respectively, while Devine and Wulff (1975) reported them to be 20% and 35%, respectively. The Mo content measured by Kilner et al. (1982) was similar to Devine and Wulff's results (Devine and Wulff, 1975), but the Cr content was 59%.

Clearly a more thorough understanding of the hard phases in the CoCrMo system is desired. In this paper, the carbides in both cast and wrought conditions are examined using electron diffraction techniques and the influence of different carbides on the wear performance is briefly discussed. We will also return, briefly, in the discussion to the issue of why different microstructures have been observed by different groups, suggesting that this is due to sluggish kinetics.

2. Experimental details

2.1. Materials

A number of different samples were analyzed. Initial work was done with a commercial high-carbon wrought alloy (ASTM F1537-94) and two retrieved MOM hip implant pairs (Depuy Orthopedics) of unknown state of heat treatment made of cast high-carbon CoCrMo alloy (ASTM F75-98). The two retrieved replacements served in patients for 604 days (age: 59 years) and 14.1 years (age: 90.7 years), respectively. The implant pairs were retrieved due to loosening of the acetabular component. Based in large part on the results obtained from these samples, the microstructure evolution of two additional samples were analyzed. In particular, the wrought alloy was re-melted in an argon atmosphere and cooled using two different treatments: (i) the melt was cooled in a water-chilled copper crucible to room temperature in ~30 s; and (ii) the melt was furnace cooled to room temperature in ~2 h. The cooling rates were ~50 °C/s for the former and ~0.2 °C/s for the latter.

2.2. Material characterization

The alloys were sectioned using a high-speed abrasive saw and mechanically polished using 0.3 μm alumina powder to a mirror finish. For general grain size analysis the surfaces were etched in a solution of 50 ml water + 50 ml HCl + 4 g $K_2S_2O_5$ for 30 s at room temperature. The surfaces were then examined with an optical microscope as well as a Hitachi S3400 scanning electron microscope (SEM) operated at 20 kV. The localized mechanical properties were examined using a Hysitron Tribo-indenter with a Berkovich-type diamond indenter at a maximum load of 4 mN. For these measurements the surface was scanned in atomic force microscopy (AFM) mode before and after the indentation.

Any indentations at the phase boundaries were discarded. The average hardness and standard deviation are reported.

TEM thin foils were prepared using an FEI Helios dual beam focused ion beam (FIB). A protective platinum layer was coated on the region of interest, and a rectangle of $20\ \mu\text{m} \times 2\ \mu\text{m} \times 6\ \mu\text{m}$ was cut out with a gallium ion beam at 30 kV. The thin piece was then attached to an Omniprobe TEM grid, followed by thinning to $\sim 100\ \text{nm}$ with 5 kV ions. A Hitachi HD2300 TEM/STEM equipped with an energy dispersive X-ray spectrometer (EDS) operated at 200 kV was used for elemental mapping.

A JEOL 2100F TEM operated at 200 kV was employed to identify the crystallographic structure by examining either select area diffraction (SAD) or nano-beam diffraction (NBD) patterns. These two techniques, however, involve strong dynamical diffraction particularly for thick specimens. As a result, diffraction intensities are usually different from what is predicted by the kinematical theory, which significantly complicates the analysis. In order to ease the solutions of structure, we used precession electron diffraction (PED) (Vincent and Midgley, 1994), to obtain pseudo-kinematical patterns. Fig. 1 shows a diagram of the PED system at Northwestern University. The system generates a serial conical illumination rocking on the area of interest, combining a complementary post-specimen descann bringing spinning diffraction beams to spots. The semi-cone angle was set to 23.7 mrad. Detailed information of the setup has been described elsewhere (Own et al., 2005). Because the Bragg reflections are collected in off-zone conditions, dynamical scattering is greatly reduced. For reference, the PED method is relatively new and has proved to be a very powerful approach to obtaining crystallographic information within a transmission electron microscope, in most cases rather superior to older fixed-beam diffraction techniques. For some recent publications see Ciston et al. (2008), Gemmi et al. (2010), Gjonnes et al. (1998a, 2004), Gjonnes (1997), Gjonnes et al. (1998b), Hadermann et al. (2010, 2011), Meshi et al. (2011), Moeck and Rouvimov (2010), Own et al. (2006a,b), Rauch et al. (2010), Schurmann et al. (2011), Sinkler and Marks (2010) and Sinkler et al. (2007).

3. Results

3.1. Cast alloy

Fig. 2(a) shows an optical micrograph of the head component made from the as-cast alloy. The specimen had typical lamellar hard phases (as we will see later they are mixtures of fine hard phases rather than single phase carbide) of $\sim 50\ \mu\text{m}$ in length within the grains and at the grain boundaries. These hard phases have a similar appearance to those reported in Refs. Caudillo et al. (2002), Dobbs and Robertson (1983), Lopez and Saldivar-Garcia (2008), Montero-Ocampo et al. (1999) and Saldivar-Garcia and Lopez (2005). Several pits were observed inside the hard phases, which were presumably formed during the mechanical polishing and/or etching. The cup component, also made of the as-cast alloy, had grain boundaries with a typical grain size of a few millimeters, as shown in Fig. 2(b); the inset shows an SEM micrograph

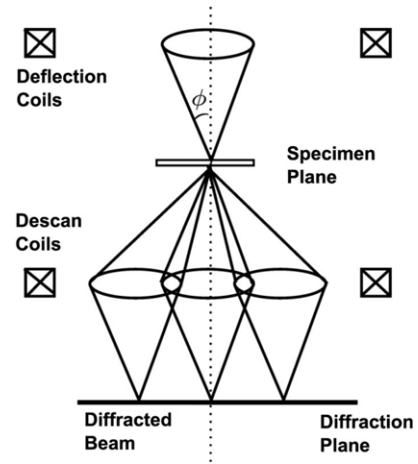


Fig. 1 – Simplified schematic of precession geometry. Source: Modified from Own et al. (2006a).

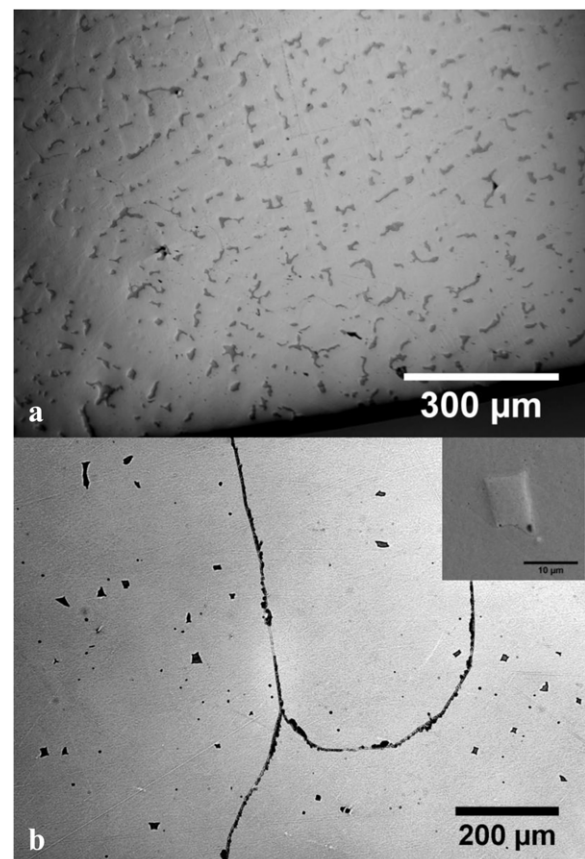


Fig. 2 – Optical micrograph of the (a) head and (b) femoral cup made of the cast alloy. The inset in (b) is a SEM image at higher magnification of a hard phase region within the cup.

of a hard phase at a higher magnification. The hard phases in the cup component were on the order of $5\ \mu\text{m}$, smaller than those in the head component, and were found mostly within the grains with straight phase boundaries. Pits were also observed in the cup component.

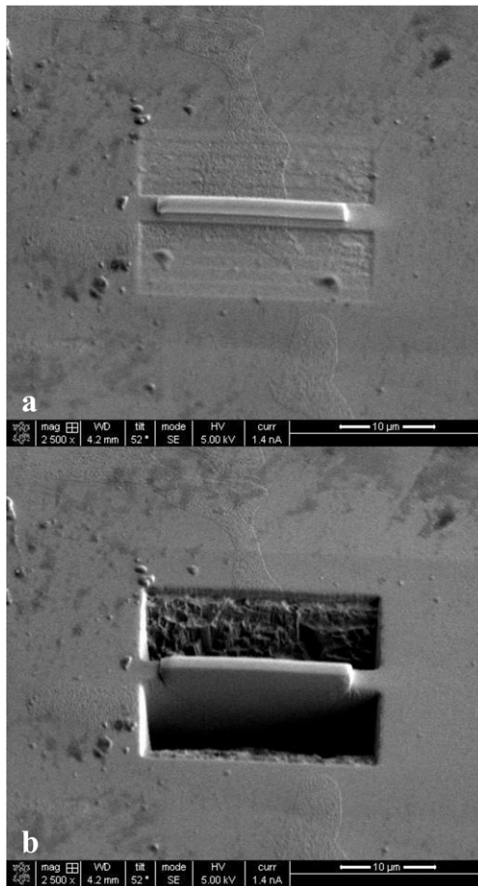


Fig. 3 – SEM image of preparation of a TEM specimen of a hard phase from the head component. (a) A platinum layer $\sim 2 \mu\text{m}$ thick was deposited on the phase and (b) a thin foil was cut using a gallium ion beam.

TEM specimen preparation of a hard phase from the head component is illustrated with the SEM micrographs in Fig. 3. (For completeness, we note that the hard phase was protected by a $\sim 2 \mu\text{m}$ thick platinum layer during sample preparation.) Fig. 4(a) shows a TEM micrograph of the hard phase from the head component. Interestingly, it was composed of very fine grains of about 100 nm. Fig. 4(b) shows a phase boundary between the matrix and carbides, which was found to be a few nanometers thick. A number of stacking faults (which show classic fringe contrast in a TEM image) were present in the matrix. Fig. 4(c) shows a typical electron diffraction pattern of an individual nm-size grain taken along the [01-1] zone axis. The nanophases have a cubic structure with a lattice parameter of 1.092 nm, which is likely to be M_{23}C_6 -type carbide; but this is not definitive. The carbides of the cup component, despite appearing smaller, are similar to those in the head component and feature $\sim 100 \text{ nm}$ nanograins, see Fig. 4(d).

As stated previously, it is complicated and somewhat dangerous to solve crystal structure using regular SAD/NBD diffraction due to the strong dynamical diffraction of electrons. We therefore used PED with either parallel nano-beam or converged beam illumination. Fig. 5(a) and (b) show PED converged beam electron diffraction (CBED) and spot

Table 1 – Chemical composition of the four regions marked in Fig. 6. The standard deviation is listed.

Wt%	Cr	Co	Mo
1	57.14 (0.54)	28.62 (0.48)	14.24 (0.77)
2	62.57 (0.59)	30.53 (0.53)	6.90 (0.59)
3	22.11 (0.38)	75.05 (0.79)	2.85 (0.45)
4	22.27 (0.54)	43.74 (0.85)	33.99 (1.65)

diffraction patterns of typical nanograins near the [011] zone, respectively. The integration over incident directions makes the pattern appear to be at the zone axis, a well-established effect. A simulated Cr_{23}C_6 carbide pattern based on kinematical theory is shown in Fig. 5(c). The intensities of the PED patterns can be readily compared to the simulated patterns as expected (Gjonnes, 1997; Own et al., 2006b), for example the {04-4} and {33-3} diffractions display relatively strong intensity while {02-2} and {11-1} are dim. It is evident that the grain is M_{23}C_6 -type carbide. While most of the nanograins were determined to have a M_{23}C_6 -structure, a few fcc nanophases similar to the matrix were also observed in the hard phases.

Fig. 6 shows a bright-field TEM micrograph of the carbide from the head component along with the corresponding elemental mappings (Co, Cr and Mo). The chemical composition of the nanograins in the carbides varied significantly, indicating poor homogeneity of the mixed hard phases even for grains having the same M_{23}C_6 crystallographic structure. The compositions of regions 1–4 labeled in Fig. 6(b) are listed in Table 1. In general, the nanograins were compositionally divided into two categories: some grains contained a relatively high Co content, while the others were Cr-rich.

3.2. Wrought alloy

Fig. 7 shows an optical micrograph of the wrought alloy. The matrix grain size was a few microns, with $\sim 1 \mu\text{m}$ large carbides distributed uniformly within the grains and at the grain boundaries. The TEM micrograph in Fig. 8(a) shows that the internal carbide structure is homogeneous. Based on the electron diffraction pattern in Fig. 8(b), it was determined that these carbides are of M_{23}C_6 -type with a lattice parameter of 1.066 nm. The chemical composition of the carbide in the wrought alloy was measured by EDS to be $\text{Co}_{14}\text{Cr}_{72}\text{Mo}_{14}$ (in wt%) with error of about 1%.

Localized hardness and modulus of both the mixed hard phases and homogeneous M_{23}C_6 carbides were measured using nanoindentation. Despite the differences in the microstructural appearance, the mechanical properties of the mixed hard phases in the head and cup components made of as-cast alloy were similar. This is not surprising, as both carbides were composed of nanograins. Fig. 9(a) and (b) show AFM micrographs of the hard phases in the cast alloy head component and the wrought alloy after indentation tests. Typical force–displacement curves are shown in Fig. 9(c). The hardness and modulus were determined using the

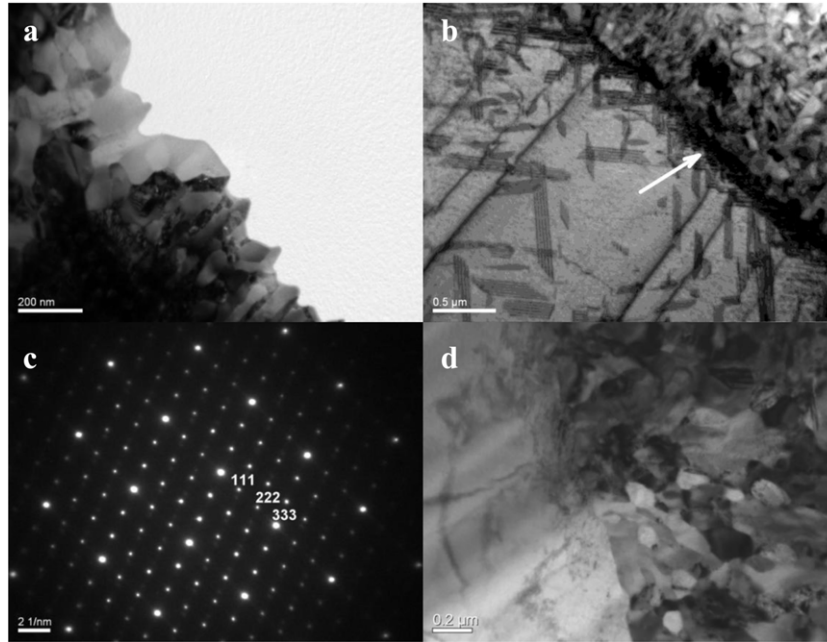


Fig. 4 – Bright-field TEM micrographs of (a) the hard phase within the head component of the cast alloy showing nanograins, and (b) the phase boundary (arrowed) of the CoCrMo matrix and hard phases. Stacking faults with standard fringe contrast were present the matrix. (c) Electron diffraction pattern of a single nanograin along the $[01-1]$ zone axis. (d) The hard phase within the cup component is also composed of nanograins.

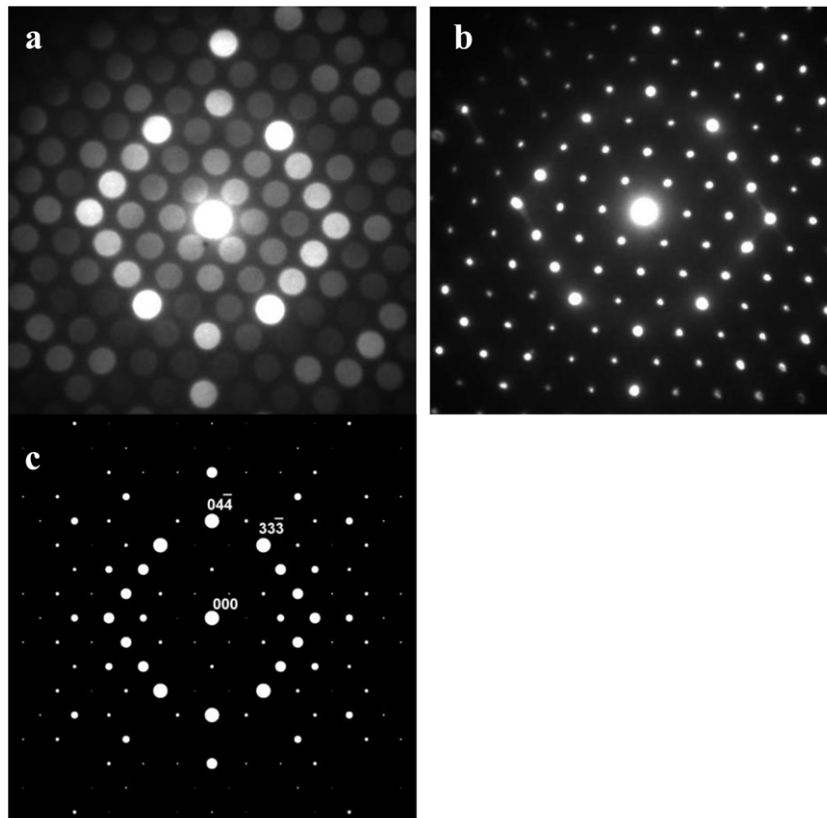


Fig. 5 – (a) Precessed CBED pattern and (b) spot diffraction pattern; the zone axis is near $[011]$. (c) Simulated kinematical diffraction pattern.

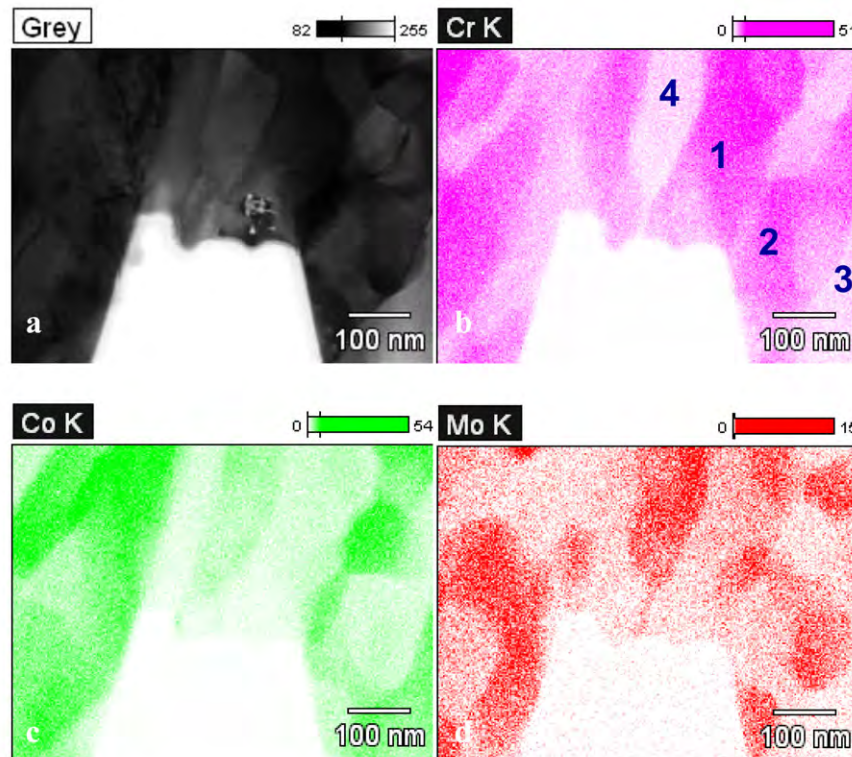


Fig. 6 – (a) Bright-field image of mixed fine structures in the cast alloy. (b) Cr, (c) Co and (d) Mo elemental mapping using EDS. The chemical composition of regions 1–4 are listed in Table 1.

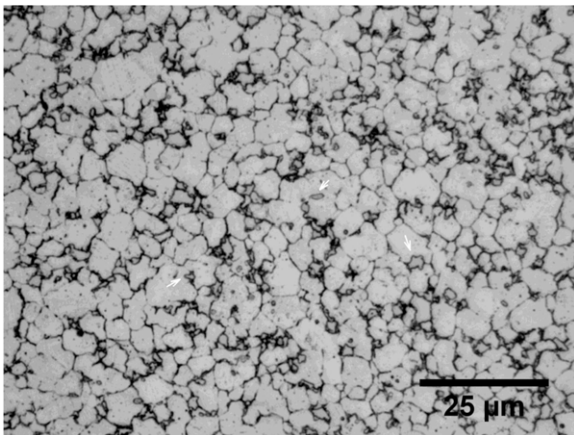


Fig. 7 – Optical micrograph showing grain size refined to a few microns in the wrought alloy. Carbides of 0.5–1 μm (as arrowed in the micrograph) were uniformly distributed in the matrix.

Oliver–Pharr model, by fitting the unloading curves using the power law (Oliver and Pharr, 1992):

$$P = C(h - h_f)^m$$

where h_f is the maximum depth after unloading and C and m are material constants (Oliver and Pharr, 1992). The hardness and modulus of the hard phase mixture in the cast alloy were determined to be 15.7 ± 0.9 GPa and 269 ± 6 GPa, respectively. The hardness of the matrix in the cast alloy was 6.4 ± 0.3 GPa. For comparison, the hardness and modulus

of the carbides in the wrought alloy were 30.7 ± 2.6 GPa and 309 ± 16 GPa, respectively, whilst the hardness of the wrought alloy's matrix was 9.4 ± 0.8 GPa. The carbides in the wrought alloy are nearly twice as hard as those of the mixed hard phases in the cast alloy. It can be seen from the unloading curves in Fig. 9(c) that the carbides in the wrought alloy underwent less plastic deformation than the mixed hard phases in the cast alloy.

3.3. Microstructures cooled at different rates

The detailed heat treatments of the cast retrieval and the wrought alloy were not available, which limits understanding of why the different microstructures arise. In order to unravel the origin of the different carbide phases, the wrought alloy was remelted and cooled at either 50°C/s or 0.2°C/s . Fig. 10(a) shows an optical image of the specimen cooled at 0.2°C/s . Blocky hard phases were observed to be ~ 200 μm long and ~ 15 μm wide. A TEM micrograph of the hard phase made using FIB is shown in Fig. 10(b). The phase is composed of ~ 100 nm fine structures, similar to the mixed hard phases in the as-cast alloy, and the chemical compositions of the nanostructure varies for each nanostructure. The chemical compositions of area 1 (Cr rich) and 2 (Mo rich) are listed in Table 2.

An optical micrograph of the hard phases in the specimen cooled at 50°C/s is shown in Fig. 11(a). The carbide phases were 5–10 μm single phases, see Fig. 11(b). Table 2 shows the chemical compositions of the single phase carbides, which contained more Mo (23.16%) than the matrix (6.87%).

Table 2 – Chemical compositions of the hard phases and matrices cooled at different rates.

	Wt%	Cr	Co	Mo
Cooled at 0.2 °C/s (Fig. 10(b))	Nanophase 1	56.55 (1.34)	18.54 (0.76)	24.91 (1.59)
	Nanophase 2	20.51 (0.75)	27.27 (0.92)	52.22 (1.30)
	Matrix	24.02 (0.81)	68.33 (1.24)	7.66 (1.35)
Cooled at 50 °C/s	Single phase carbide	32.07 (0.56)	44.77 (0.68)	23.16 (0.90)
	Matrix	64.74 (0.44)	28.39 (0.33)	6.87 (0.47)

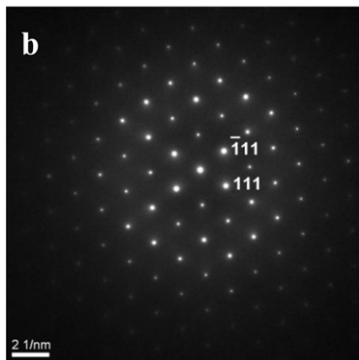
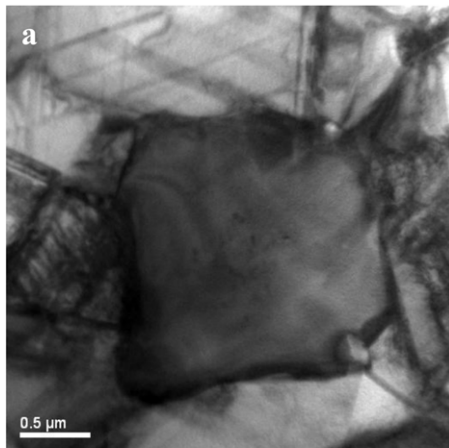


Fig. 8 – (a) Bright-field TEM micrograph of a carbide in the wrought alloy. (b) Electron diffraction pattern along the [01-1] zone axis.

The hardnesses of the mixed hard phase and the matrix of the specimen cooled at 0.2 °C/s were 15.7 ± 9 GPa and 6.4 ± 3 GPa, respectively, which are close to those of the cast retrieval. For the specimen cooled at 50 °C/s, the hardness is 16.3 ± 0.9 GPa for the single phase carbide and 6.2 ± 0.3 GPa for the matrix. The mechanical properties of the hard phases are summarized in Table 3.

4. Discussion

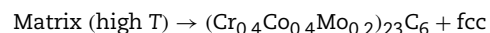
$M_{23}C_6$ carbides are the dominant hard phase in both cast and wrought CoCrMo alloys. Transformation from $M_{23}C_6$ to

Table 3 – Nano-hardness of the phases of CoCrMo alloys (unit: GPa). The numbers of measurement are shown in the brackets.

	Hard phase	Matrix
Cooled at 0.2 °C/s	15.0 ± 2.2 (34)	6.1 ± 0.3 (22)
Cooled at 50 °C/s	16.3 ± 0.9 (8)	6.2 ± 0.3 (31)
The retrieval made of cast alloy	15.7 ± 9 (7)	6.4 ± 3 (8)
Wrought	30.7 ± 2.6 (7)	9.4 ± 0.8 (11)

M_6C , as suggested by Clemow and Daniell (1979), was not observed. Although the carbides investigated in this study have the same $M_{23}C_6$ -type crystallographic structure, they exhibited different structural and mechanical properties. The mixed hard phases found in the head component made of the cast alloy appeared to be blocky ($\sim 50 \mu m$) with an elongated morphology, while those found in the cup component appeared to be on the order of a few microns. Despite the smaller size in the cup component, the mixed hard phases in both head and cup were mixtures of three phases, i.e. the fcc phase similar to the matrix, Co-rich $M_{23}C_6$ carbide, and Mo-rich $M_{23}C_6$ carbides. The two kinds of carbide have similar nanohardnesses of about 15.7 GPa. The carbides in the wrought alloy, on the other hand, were a few microns large $M_{23}C_6$ single phases. This is consistent with the electron microprobe measurements, in which wrought alloys exhibited a higher degree of homogeneity than cast alloys (Devine et al., 1972) and Clemow and Daniell (1979) measured the chemical compositions and reported little Mo segregation (variation $<2\%$) across cast alloys. Therefore the Mo-rich $M_{23}C_6$ carbide in the mixed hard phase should not be due to segregation during casting.

Our hypothesis is that a single phase $M_{23}C_6$ carbide is metastable and precipitates during fast-cooling:



where the compositions used are based upon the EDS results shown earlier for the fast-cooled alloy. A mixed hard phase consisting of crystallographically-identical but chemically-different $M_{23}C_6$ carbides is thermodynamically stable. However, the precipitation of the mixed hard phase is

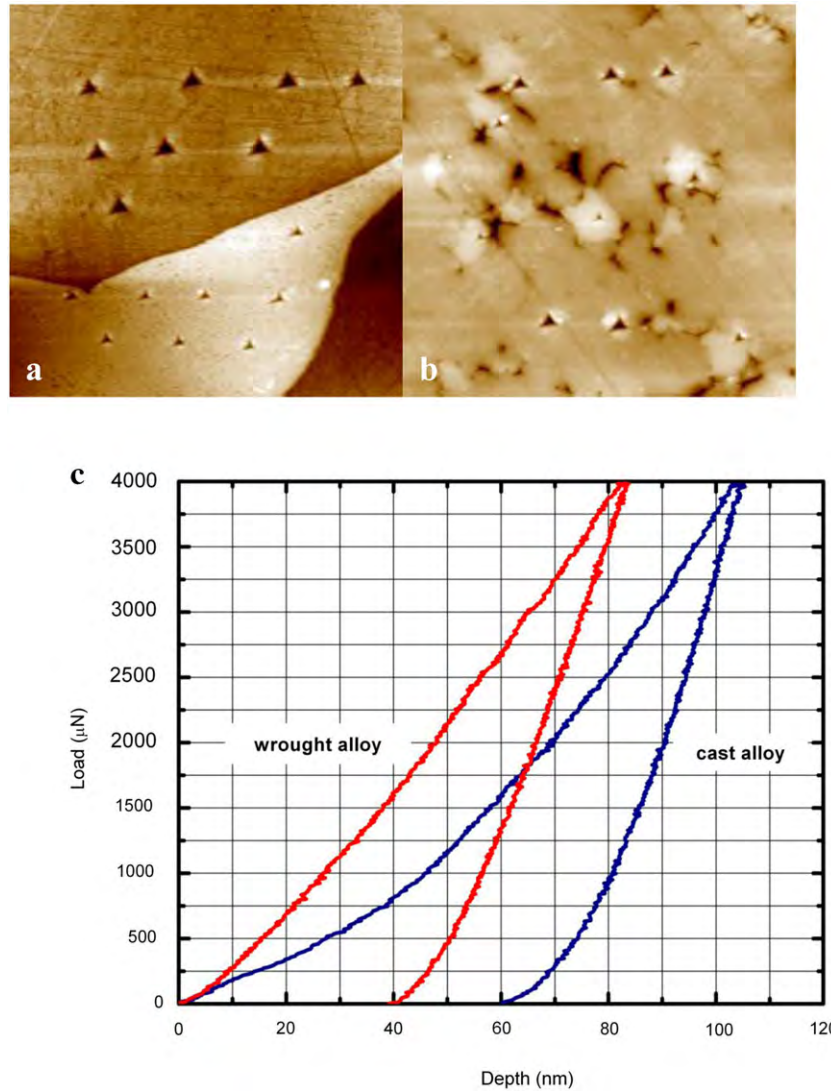
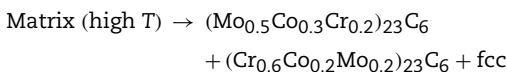


Fig. 9 – AFM image of indents in the (a) cast alloy and (b) wrought alloy. The scanning areas were $20\ \mu\text{m} \times 20\ \mu\text{m}$. The indentation size in cast alloy is greater than that in wrought alloy. The corresponding force–displacement curves are showed in (c). The wrought alloy carbide underwent less plastic deformation.

sluggish and only occurred with a slow-cooling rate:



and the compositions are again based upon the earlier EDS results for the slow-cooled alloy. We note that annealing of these samples at $1230\ \text{°C}$ for 1 h coarsened the two carbides but did not change the compositions which implies that these are thermodynamically stable. They are also consistent with the retrievals made from a cast alloy. It has been shown that Mo_{23}C_6 has a lower Gibbs free energy than Cr_{23}C_6 below $700\ \text{°C}$ (see Table 3 in Ref. Senior, 1988), and Mo partitioning in M_{23}C_6 took place during aging of CrMoV steels (Senior, 1988). In fact, M_{23}C_6 carbides frequently coexist with either M_3C (Senior, 1988) or M_6C carbides (Kuo and Jia, 1985) in annealed CrMoV steels, which is consistent with sluggish kinetics. We note that for the somewhat similar CrMoV steels a large scatter of precipitate compositions and structures have been

reported (Senior, 1988) which is consistent with variations due to slightly different annealing treatments. This is also consistent with the scatter in results for the CrCoMo system mentioned in the introduction.

The hardness of the carbide in wrought alloy was about twice that of the cast alloy. Devine et al. reported that wrought alloys had better mechanical properties and resistance to crevice corrosion (Devine et al., 1972). The yield strength of the wrought alloy was 689 MPa compared with 551 MPa for cast alloys, whereas the total elongation of wrought alloy was 26% compared to 8% for the cast alloy (Devine et al., 1972). It is worth noting that the influence of hard phases is complicated as sliding wear is determined by many metallurgical properties simultaneously such as hardness, ductility, modulus, etc. (Zum Gahr, 1987). It has been reported that hard carbides promote the strength and resistance against abrasive wear (Antony, 1983; Gomez et al., 1997; Pourzal et al., 2009), thus the wrought alloy is expected to be stronger as its M_{23}C_6 carbide precipitates are harder than the

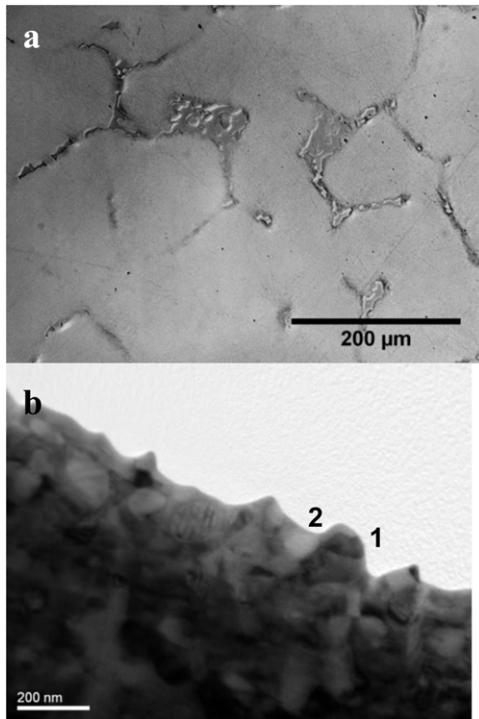


Fig. 10 – (a) Optical and (b) TEM micrographs of the specimen cooled at 0.2 °C/s. The hard phases are composed of ~100 nm fine structures.

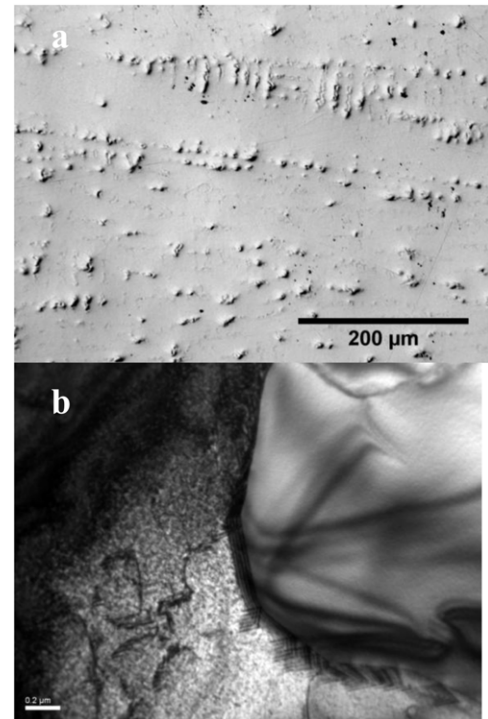


Fig. 11 – (a) Optical micrograph of the specimen cooled at 50 °C/s. The hard phases are 5–10 μm large. (b) TEM micrograph showing that the hard phase is single phase carbide.

mixed hard phases in the cast alloy. The SEM micrographs in Fig. 12(a) and (b) show the cross-section of the retrieved implant made of the cast alloy. Fracture of the coarse mixed hard phases near the surface or phase boundary cracks was frequently observed, while no discernible fracture occurred in the matrix. For comparison, the single phase carbides in a wrought alloy tests remained intact after 5 million cycles simulator tests, see Fig. 12(c). It is clear that the fracture of the coarse carbides consisting of nanograins in the cast metal hip implant should be avoided.

In addition to the mechanical performance of the hip implants, bioactive particulate CoCrMo nanoparticles generated during the wear processes are of concern recently as they have been associated with adverse local tissue responses (Jacobs et al., 2009). While the nanoparticles may originate from the nanocrystalline layer at CoCrMo alloy surfaces formed via large plastic deformation and dynamical recrystallization as shown by Buscher and Fischer (2005), the mixed hard phases observed in cast alloys may serve as additional nanoparticle sources Doorn et al. (1998) isolated metal particles from tissues and reported that the particle size ranged from 20 to 834 nm with the median of 81 nm. The particle sizes and geometry were similar to the nanograins observed in the cast alloy carbides. Wimmer et al. (2001) showed that carbide/carbide contacts under high local stress could result in carbide fracture and spalling out from the surfaces. As showed in the schematic in Fig. 13, sliding on the protruded mixed hard phases may lead to the detachment of the nanograins, producing loose nanoparticles. As noted in the optical images, pitting occurred frequently at the mixed

hard phases in cast specimens, indicating that nanograins could be spalled out. In simulated tests, Catelas et al. (2003) observed roughly twice as many wear metal nanoparticles of ~53 nm from cast alloy bearings compared to wrought alloy bearings; this may be partly due to the nanograins spalling out as well. Thus, it may be of interest to eliminate the mixed hard phases for CoCrMo alloys used for implants. It is worth noting that the mixed hard phases may not be distinguishable from a $M_{23}C_6$ single phase carbide by XRD alone, since the most of the nanograins have similar $M_{23}C_6$ lattice structures.

One final point of discussion: it should be clear that while the different formation processes (cast versus wrought) produce similar materials, they are certainly not the same and one should expect some differences during use in-vivo because of different load-bearing, wear and friction (when there is no triboactive lubricant graphitic layer Liao et al., 2011) during use. Indeed, just describing the material as “cast” or “wrought” is not really correct, as it is very firmly established that fine details of heat treatments in alloys can lead to large changes in microstructure and properties. This clearly shows up in our comparison of the alloys fast- and slow-cooled. For instance, with high performance alloys used in the aerospace or automotive industries almost every step of heat treatments is precisely controlled, rather than just specifying bounds for the composition as in the current ASTM standards for Co-based alloys for implants. Hence the fact that our results do not completely match what has been reported by others and the fact that variations have been reported in the literature is to be expected, when

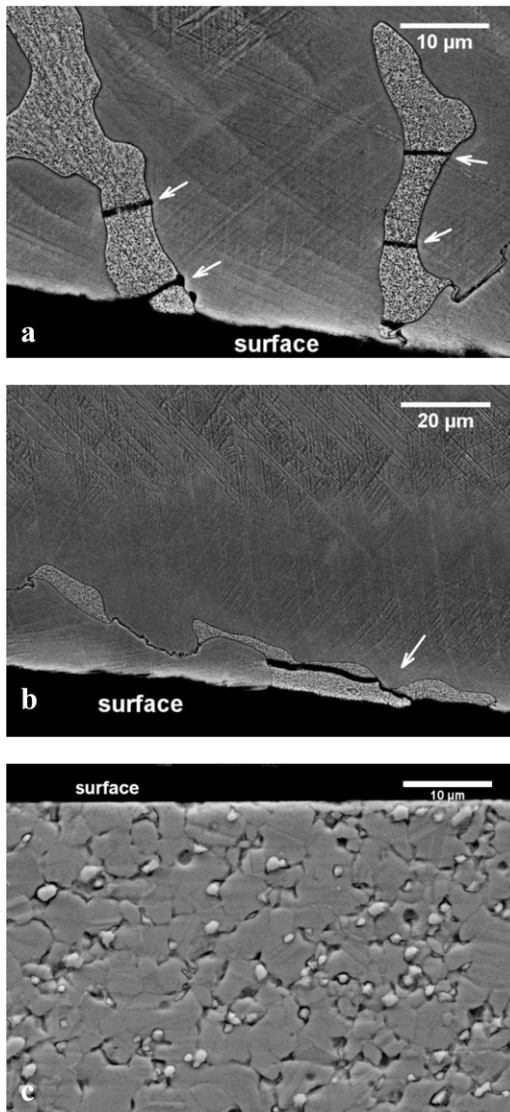


Fig. 12 – (a) and (b) Cross-section SEM micrographs of a retrieved implant (head component) made of cast alloy. Fractures of the mixed hard phases near the surface frequently occurred as arrowed in the images. (c) The single phase carbides in a wrought alloy were intact after 5 million cycles simulator test.

there are alloys with the same nominal composition without full microstructure control. The varied microstructures may consequently lead to scattered wear rates as well as variable performance of hip replacements in-vivo or in simulated tests (Chan et al., 1999; Streicher et al., 1990). A critical treatment of the microstructure is imperative.

5. Conclusions

In the cast retrieved implant, the size of the mixed hard phases was $\sim 50 \mu\text{m}$ in the head component and $\sim 5 \mu\text{m}$ in the cup component. Hard phases composed of nanograins were found in both head and cup components. PED results

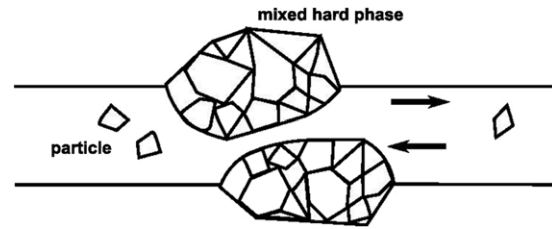


Fig. 13 – Schematic of nanoparticles generated from mixed hard phases during wear.

show that the hard phases in the cast alloy consists of mostly M_{23}C_6 -type carbides and few fcc phases. The chemical compositions varied from grain to grain. In general, the nanograins were either Co-rich or Cr-rich. The origin of the mixed hard phases was related to slow cooling during solidification. In contrast, the hard phases in the wrought condition were homogeneous M_{23}C_6 single phase. Nanoindentation measurements showed that the hardness of mixed hard phases was $\sim 15.7 \text{ GPa}$, only half that of the homogeneous carbide ($\sim 30.7 \text{ GPa}$) in the wrought alloy. It is suggested that the hard phases consisting of nanograins are detrimental to both wear performance and biocompatibility.

Acknowledgments

This research is supported by the NIH on grant number 1RC2AR058993-01 and NSF on grant number CMMI-1030703. The authors are indebted to M. Morlock, Hamburg, Germany for retrievals, and Pooja Panigrahi and Andres Becera-Toledo for proof reading the manuscript.

REFERENCES

- Antony, K.C., 1983. Wear-resistant cobalt-base alloys. *J. Met.* 35, 52–60.
- Asgar, K., Peyton, F.A., 1961. Effect of microstructure on physical properties of cobalt-base alloys. *J. Dent. Res.* 40, 63–72.
- Buscher, R., Fischer, A., 2005. The pathways of dynamic recrystallization in all-metal hip joints. *Wear* 259, 887–897.
- Catelas, I., Bobyn, J.D., Medley, J.B., Krygier, J.J., Zukor, D.J., Huk, O.L., 2003. Size, shape, and composition of wear particles from metal–metal hip simulator testing: effects of alloy and number of loading cycles. *J. Biomed. Mater. Res. Part A* 67A, 312–327.
- Caudillo, M., Herrera-Trejo, M., Castro, M.R., Ramirez, E., Gonzalez, C.R., Juarez, J.I., 2002. On carbide dissolution in an as-cast ASTM F-75 alloy. *J. Biomed. Mater. Res.* 59, 378–385.
- Chan, F.W., Bobyn, J.D., Medley, J.B., Krygier, J.J., Tanzer, M., 1999. Wear and lubrication of metal-on-metal hip implants. *Clin. Orthop. Relate. Res.* 10–24.
- Ciston, J., Deng, B., Marks, L.D., Own, C.S., Sinkler, W., 2008. A quantitative analysis of the cone-angle dependence in precession electron diffraction. *Ultramicroscopy* 108, 514–522.
- Clemow, A.J.T., Daniell, B.L., 1979. Solution treatment behavior of Co–Cr–Mo alloy. *J. Biomed. Mater. Res.* 13, 265–279.
- Devine, T.M., Wulff, J., 1975. Cast vs. wrought cobalt–chromium surgical implant alloys. *J. Biomed. Mater. Res.* 9, 151–167.

- Devine, T.M., Kummer, F.J., Wulff, J., 1972. Wrought cobalt-chromium surgical implant alloys. *J. Mater. Sci.* 7, 126–128.
- Dobbs, H.S., Robertson, J.L.M., 1983. Heat-treatment of cast Co-Cr-Mo for orthopedic implant use. *J. Mater. Sci.* 18, 391–401.
- Doom, P.F., Campbell, P.A., Worrall, J., Benya, P.D., McKellop, H.A., Amstutz, H.C., 1998. Metal wear particle characterization from metal on metal total hip replacements: transmission electron microscopy study of periprosthetic tissues and isolated particles. *J. Biomed. Mater. Res.* 42, 103–111.
- Gemmi, M., Klein, H., Rageau, A., Strobel, P., Le Cras, F., 2010. Structure solution of the new titanate $\text{Li}_4\text{Ti}_8\text{Ni}_3\text{O}_{21}$ using precession electron diffraction. *Acta Crystallogr. Sect. B* 66, 60–68.
- Gjonnes, K., 1997. On the integration of electron diffraction intensities in the Vincent-Midgley precession technique. *Ultramicroscopy* 69, 1–11.
- Gjonnes, J., Hansen, V., Berg, B.S., Runde, P., Cheng, Y.F., Gjonnes, K., Dorset, D.L., Gilmore, C.J., 1998a. Structure model for the phase AlmFe derived from three-dimensional electron diffraction intensity data collected by a precession technique. Comparison with convergent-beam diffraction. *Acta Crystallogr. Sect. A* 54, 306–319.
- Gjonnes, K., Cheng, Y.F., Berg, B.S., Hansen, V., 1998b. Corrections for multiple scattering in integrated electron diffraction intensities. Application to determination of structure factors in the [001] projection of AlmFe . *Acta Crystallogr. Sect. A* 54, 102–119.
- Gjonnes, J., Hansen, V., Kverneland, A., 2004. The precession technique in electron diffraction and its application to structure determination of nano-size precipitates in alloys. *Microsc. Microanal.* 10, 16–20.
- Gomez, M., Mancha, H., Salinas, A., Rodriguez, J.L., Escobedo, J., Castro, M., Mendez, M., 1997. Relationship between microstructure and ductility of investment cast ASTM F-75 implant alloy. *J. Biomed. Mater. Res.* 34, 157–163.
- Hadermann, J., Abakumov, A.M., Tsirlin, A.A., Filonenko, V.P., Gonnissen, J., Tan, H.Y., Verbeeck, J., Gemmi, M., Antipov, E.V., Rosner, H., 2010. Direct space structure solution from precession electron diffraction data: resolving heavy and light scatterers in $\text{Pb}_{13}\text{Mn}_9\text{O}_{25}$. *Ultramicroscopy* 110, 881–890.
- Hadermann, J., Abakumov, A.M., Turner, S., Hafideddine, Z., Khasanova, N.R., Antipov, E.V., Van Tendeloo, G., 2011. Solving the structure of Li ion battery materials with precession electron diffraction: application to $\text{Li}_2\text{CoPO}_4\text{F}$. *Chem. Mater.* 23, 3540–3545.
- Hutchings, I.M., 1992. *Tribology: Friction and Wear of Engineering Materials*. Edward Arnold, London.
- Jacobs, J.J., Urban, R.M., Hallab, N.J., Skipor, A.K., Fischer, A., Wimmer, M.A., 2009. Metal-on-metal bearing surfaces. *J. Am. Acad. Orthop. Surg.* 17, 69–76.
- Kilner, T., Pilliar, R.M., Weatherly, G.C., Allibert, C., 1982. Phase identification and incipient melting in a cast Co-Cr surgical implant alloy. *J. Biomed. Mater. Res.* 16, 63–79.
- Kuo, K.H., Jia, C.L., 1985. Crystallography of M23c6 and M6c precipitated in a low-alloy steel. *Acta Metall. Mater.* 33, 991–996.
- Kurtz, S., Ong, K., Lau, E., Mowat, F., Halpern, M., 2007. Projections of primary and revision hip and knee arthroplasty in the United States from 2005 to 2030. *J. Bone Joint Surg. Am.* 89A, 780–785.
- Liao, Y., Pourzal, R., Wimmer, M.A., Jacobs, J.J., Fischer, A., Marks, L.D., 2011. Graphitic tribological layers in metal-on-metal hip replacements. *Science* 334, 1687–1690.
- Lopez, H.F., Saldivar-Garcia, A.J., 2008. Martensitic transformation in a cast Co-Cr-Mo-C alloy. *Metall. Mater. Trans. A* 39A, 8–18.
- Meshi, L., Samuha, S., Kapush, D., Pavlyuchkov, D., Grushko, B., 2011. New complex intermetallic in the Al-Rh-Ru alloy system. *J. Alloys Compd.* 509, 6551–6555.
- Moeck, P., Rouvimov, S., 2010. Precession electron diffraction and its advantages for structural fingerprinting in the transmission electron microscope. *Z. Krist.* 225, 110–124.
- Montero-Ocampo, C., Talavera, M., Lopez, H., 1999. Effect of alloy preheating on the mechanical properties of as-cast Co-Cr-Mo-C alloys. *Metall. Mater. Trans. A* 30, 611–620.
- Oliver, W.C., Pharr, G.M., 1992. An improved technique for determining hardness and elastic modulus using load and displacement sensing indentation experiments. *J. Mater. Res.* 7, 1564–1583.
- Own, C.S., Marks, L.D., Sinkler, W., 2005. Electron precession: a guide for implementation. *Rev. Sci. Instrum.* 76.
- Own, C.S., Marks, L.D., Sinkler, W., 2006a. Precession electron diffraction 1: multislice simulation. *Acta Crystallogr. Sect. A* 62, 434–443.
- Own, C.S., Sinkler, W., Marks, L.D., 2006b. Rapid structure determination of a metal oxide from pseudo-kinematical electron diffraction data. *Ultramicroscopy* 106, 114–122.
- Poggie, R.A., Afflitto, R.M., John, K.S., The wear performance of precision Co-Cr-Mo alloy metal-on-metal hip bearings, in: *Proceedings of the Conference Transactions of the 12th Annual International Symposium for Technology in Arthroplasty*, Chicago, 1999, pp. XI:1–XI:2.
- Pourzal, R., Theissmann, R., Williams, S., Gleising, B., Fisher, J., Fischer, A., 2009. Subsurface changes of a MoM hip implant below different contact zones. *J. Mech. Behav. Biomed.* 2, 186–191.
- Rauch, E.F., Portillo, J., Nicolopoulos, S., Bultreys, D., Rouvimov, S., Moeck, P., 2010. Automated nanocrystal orientation and phase mapping in the transmission electron microscope on the basis of precession electron diffraction. *Z. Krist.* 225, 103–109.
- Saldivar-Garcia, A.J., Lopez, H.F., 2005. Microstructural effects on the wear resistance of wrought and as-cast Co-Cr-Mo-C implant alloys. *J. Biomed. Mater. Res. Part A* 74A, 269–274.
- Schurmann, U., Duppel, V., Buller, S., Bensch, W., Kienle, L., 2011. Precession electron diffraction—a versatile tool for the characterization of phase change materials. *Cryst. Res. Technol.* 46, 561–568.
- Senior, B.A., 1988. A critical-review of precipitation behavior in 1cr-Mo-V rotor steels. *Mater. Sci. Eng. A Struct.* 103, 263–271.
- Sinkler, W., Marks, L.D., 2010. Characteristics of precession electron diffraction intensities from dynamical simulations. *Z. Krist.* 225, 47–55.
- Sinkler, W., Own, C.S., Ciston, J., Marks, L.D., 2007. Statistical treatment of precession electron diffraction data with principal components analysis. *Microsc. Microanal.* 13 (Suppl. 2 Proceedings), 954CD–955CD.
- Streicher, R.M., Schon, R., Semlitsch, M.F., 1990. Investigation of the tribological behavior of metal-on-metal combinations for artificial hip joints. *Biomed. Tech.* 35, 107–111.
- Taylor, R.N.J., Waterhouse, R.B., 1986. The metallography of a cobalt-based implant alloy after solution treatment and ageing. *J. Mater. Sci.* 21, 1990–1996.
- Vincent, R., Midgley, P.A., 1994. Double conical beam-rocking system for measurement of integrated electron-diffraction intensities. *Ultramicroscopy* 53, 271–282.
- Willert, H.G., Semlitsch, M., 1977. Reactions of articular capsule to wear products of artificial joint prostheses. *J. Biomed. Mater. Res.* 11, 157–164.
- Wimmer, M.A., Loos, J., Nassutt, R., Heitkemper, M., Fischer, A., 2001. The acting wear mechanisms on metal-on-metal hip joint bearings: in vitro results. *Wear* 250, 129–139.
- Wimmer, M.A., Sprecher, C., Hauert, R., Tager, G., Fischer, A., 2003. Tribochemical reaction on metal-on-metal hip joint bearings—a comparison between in-vitro and in-vivo results. *Wear* 255, 1007–1014.
- Zum Gahr, K.H., 1987. *Microstructure and Wear of Materials*. Elsevier Science Publishers, Amsterdam, The Netherlands.